Ocean Modelling 191 (2024) 102426

Contents lists available at ScienceDirect

Ocean Modelling

journal homepage: www.elsevier.com/locate/ocemod

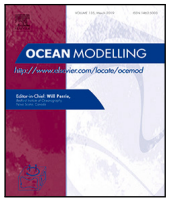

On warm bias and mesoscale dynamics setting the Southern Ocean large-scale circulation mean state

Mathias Zeller *, Torge Martin

GEOMAR Helmholtz Centre for Ocean Research Kiel, Kiel, Germany

ARTICLE INFO

Dataset link: Supplementary data to Zeller and Martin (2024): On warm bias and mesoscale dynamics setting the Southern Ocean large-scale circulation mean state. (Original data)

Keywords:
Southern Ocean
Mesoscale eddy
Heat content
Climate model
Ocean nesting
Large-scale circulation

ABSTRACT

A realistic representation of the Southern Ocean (SO) in climate models is critical for reliable global climate projections. However, many models are still facing severe biases in this region. Using a fully coupled global climate model at non-eddying (1/2°) and strongly eddying (1/10°) grid resolution in the SO, we investigate the effect of a 0.5 °C, 1.0 °C and 1.6 °C warmer than observed SO on i) the spin-up behaviour of the high-resolution simulation, and ii) the representation of main dynamical features, i.e., the Antarctic circumpolar current (ACC), the subpolar gyres, the overturning circulation and the Agulhas regime in a quasi-equilibrium state. The adjustment of SO dynamics and hydrography critically depends on the initial state and grid resolution. When initialised with an observed ocean state, only the non-eddying configuration quickly builds up a strong warm bias in the SO. The high-resolution configuration initialised with the biased non-eddying model state results in immense spurious open ocean deep convection, as the biased ocean state is not stable at eddying resolution, and thus causes an undesirable imprint on global circulation. The SO heat content also affects the large-scale dynamics in both low- and high-resolution configurations. A warmer SO is associated with a stronger Agulhas current and a temperature-driven reduction of the meridional density gradient at 45°S to 65°S and thus a weaker ACC. The eddying simulations have stronger subpolar gyres under warmer conditions while the response in the non-eddying simulations is inconsistent. In general, SO dynamics are more realistically represented in a mesoscale-resolving model at the cost of requiring an own spin-up.

1. Introduction

The Southern Ocean (SO) is an important region for the global thermohaline circulation due to the large-scale water mass transformation into Antarctic intermediate water (AAIW) at mid and Antarctic bottom water (AABW) at high latitudes (Gordon, 1986; Schmitz, 1996; Talley, 2013). AABW is only formed in four source regions around Antarctica and the SO is one of few locations where oceanic deep convection occurs (e.g., Silvano et al., 2023) and affects the global distribution of water masses by feeding into the deep overturning circulation (Johnson et al., 2008; Rae et al., 2018; Solodoch et al., 2022).

Strong westerly winds at mid to high latitudes are the dominant driver of the strong Antarctic circumpolar current (ACC) as well as large-scale stationary features such as the Weddell and Ross gyres and the Malvinas confluence zone. The zonal winds further initiate large-scale upwelling of deep water (Beadling et al., 2020) creating a strong meridional density gradient, which all leads to the formation of an intense mesoscale eddy field (Frenger et al., 2015; Patara et al., 2016). Upwelling and large-scale water mass transformation make the SO critical in the global heat and carbon budgets through its immense potential to sequester excess heat and anthropogenic CO_2 (Khatiwala et al., 2009; Frölicher et al., 2015; Zanna et al., 2019). The extent of the SO heat reservoir also affects the strength of the meridional density gradient which directly imprints on the large-scale horizontal circulation (Beadling et al., 2020). However, common climate models, including those of the Climate Model Intercomparison Project (CMIP, Eyring et al. (2016)), suffer from severe biases particularly in the SO, such as shifts in the westerly wind belt and too warm sea surface and deep ocean temperatures, which build up over the course of the model spin-up and shape the mean state (Heuze et al., 2013; Wang et al., 2014; Heuze, 2021; Wang et al., 2022).

Mesoscale eddies have been shown to significantly affect the horizontal and vertical distribution of ocean properties such as temperature, salinity and passive tracers in both observations and models (McCann et al., 1994; Stammer, 1998; Treguier et al., 2012; Gnanadesikan et al., 2015; Martin and Biastoch, 2023). Eddies play an important role in the amount of oceanic heat uptake and meridional heat transport including the regulation of warm water intrusions onto the continental shelf, which determine the melt rates of Antarctic ice shelves (Griffies

* Corresponding author.
E-mail address: mzeller@geomar.de (M. Zeller).

https://doi.org/10.1016/j.ocemod.2024.102426
Received 31 January 2024; Received in revised form 31 July 2024; Accepted 22 August 2024
Available online 31 August 2024

et al., 2015; Morrison et al., 2016). Another well-known example of their effect is the Agulhas system at the southern tip of South Africa where the warm and saline Agulhas current splits into a transient eddy component transporting heat and salt from the Indian into the Atlantic ocean (Agulhas leakage) and a mean return flow advecting heat eastward (Agulhas retroflection) (Lutjeharms and Vanballegooyen, 1988; Biastoch et al., 2008a). High velocity shear occurring in the ACC as well as near rough topography and the presence of strong baroclinic instabilities associated with upwelling leads to the formation of a large number of transient mesoscale eddies across the SO (Morrow et al., 1994; Chelton et al., 2011; Frenger et al., 2015). Thus, mesoscale eddies play a major part in setting the mean state dynamics of this region.

Explicitly resolving mesoscale dynamics in climate models instead of applying eddy parameterisations may alleviate some of the biases in the SO, e.g., SST and deep ocean temperature. An approach to investigate the effect of mesoscale dynamics in coupled and forced ocean models is the implementation of a secondary, regionally limited grid of refined horizontal resolution into the coarser global ocean domain, referred to as nesting (Debreu et al., 2008; Biastoch et al., 2008b). Such nests explicitly resolve processes that are not resolved in the coarser ocean grid and can interact with the global ocean in both directions, i.e., taking boundary conditions from the global ocean and feeding back information on otherwise unresolved processes. Typically, ocean (and climate) simulations require a sufficiently long, millennial spin-up run to minimise model drift owing to the ocean's large thermal and dynamical inertia. Mesoscale eddies, however, have an average diameter of about 40 km in high-latitude regions (Frenger et al., 2015) and shrink in size towards the Antarctic continent as the Rossby radius decreases (Hallberg, 2013). Thus, the immense computational costs of eddying ocean simulations, also nested and thus regionally limited ones, often prohibit simulations extending beyond a couple of centuries. The spin-up period in HighResMIP, for instance, was limited to only 30 years (Roberts et al., 2019). In particular, the investigation of deep convection and the deep overturning circulation in the SO requires a much longer spin-up period to allow for the very slow dynamics at depth to reach an equilibrium.

To ease the computational burden, a standard procedure is to run the non-eddying model (no nest) into an equilibrium state and then initialise a nested simulation from the non-nested control state. This procedure has been successfully done for nests implemented outside the SO (Ivanciu et al., 2022; Schulzki et al., 2022; Martin and Biastoch, 2023). We show here that the same procedure can fail in a nested Southern Ocean setting when the long coarse-resolution spin-up simulation used for initialisation has accumulated strong regional biases in heat content. Initialising a high-resolution eddying ocean model, which otherwise would converge to a much less biased mean state, has the potential to distort the hydrography and associated dynamic response resulting in long-lasting implications on the global circulation. The present study follows two objectives: Firstly, we investigate the impact of three initial ocean states (no, weak, and strong warm bias) on the temperature distribution (as an indicator of heat content), deep convection and large-scale circulation during an initial transient phase of high-resolution simulations comparing the effect of explicitly simulated versus parameterised eddies. Secondly, after the SO has reached a quasi-equilibrium after 100 years in each simulation, we systematically explore the impact of resolved mesoscale dynamics under different heat content mean states of the SO on a number of key quantities in the region, i.e. upper and deep ocean heat content, deep convection, the meridional density gradient and various circulation features, namely, the ACC, the subpolar gyres and the Agulhas current.

In Section 2, we describe the climate model and introduce the experimental setup of this study. The presentation of results in Section 3 is divided into two parts: the first part is concerned with the sensitivity of the high-resolution model spin-up to different initial conditions, while the second part deals with the large-scale effects of resolved mesoscale dynamics on the mean state of the SO under varyingly warm conditions. The results are discussed and conclusions are drawn in Section 5.

2. Methods

2.1. Model configuration

We employ the coupled climate model FOCI (Flexible Ocean Climate Infrastructure, Matthes et al. (2020)). The atmosphere component ECHAM6 (Stevens et al., 2013) is run at a T63/L95 resolution and is coupled to the land model JSBACH (e.g., Giorgetta et al., 2013). The ocean component is based on the Nucleus for European Modelling of the Ocean (NEMO3.6, Madec and the NEMO team (2016)) which is run on the tripolar Arakawa-C grid ORCA05 grid with a Mercator horizontal resolution of 1/2° and 46 vertical z-levels. The vertical resolution ranges from 6–17 m in the upper 100 m to 200–250 m below a depth of 2000 m. For non-eddying grid resolutions, eddy processes are parameterised using the GM scheme (Gent and McWilliams, 1990), considering the temporally and horizontally varying growth of baroclinic instabilities but capped at 2000 m^2/s (Treguier et al., 1997). Vertical mixing is handled by a 1.5 turbulent closure scheme applying a constant background eddy diffusivity of 10^{-5} m^2/s. The ocean is coupled to the sea ice model LIM2 (Fichefet and Morales Maqueda, 1997) computing ice dynamics and thermodynamic ice as well as snow processes considering three static layers. No flux correction or restoring is applied to any model component. Flux exchange between atmosphere and ocean components is facilitated using the OASIS3-MCT coupler (Valcke et al., 2016).

Focusing on mesoscale dynamics in the SO, we implemented regional grid refinement by employing 2-way nesting in the ocean using the Adaptive Grid Refinement in Fortran (AGRIF) library (Debreu et al., 2008). We implement a quasi-circumpolar nest in FOCI—only a small gap between 72°–73°E exists due to technical limitations of the model infrastructure—spanning the entire ocean south of 28°S and call this configuration FOCI-ORION10X (Fig. 1). The nest has a horizontally refined resolution of 1/10°, which equals a nominal grid spacing of 11 km but actual resolution increases as the grid converges toward the Antarctic coast to 2.5 km in longitudinal direction. A limitation of the ocean model is not simulating ice–shelf interaction and cavity circulation. AGRIF enables two-way interaction between the regional nest and the host (or parent) global model, i.e., the global model provides the nest with boundary conditions and is updated by the more accurate 3-D state of the nest in the refinement region. Atmospheric coupling is based on the coarser global grid where both the host and nest grids receive the same surface fluxes. The GM eddy parameterisation is only applied to the coarser host model outside of the nested domain and is omitted for the gap at 72°–73°E to improve eddy passage and re-entry into the nest.

2.2. Model experiments

The suite of model runs used for this study originates from the tuning phase of FOCI and FOCI-ORION10X and is an opportunity to shed light on difficulties and sensitivities associated with the SO warm bias, typical for coupled climate models. All simulations are performed under pre-industrial control conditions with constant 1850 greenhouse gas and aerosol forcing. Exploring ways to initialise FOCI-ORION10X yielded three equivalent sets of experiments, each comprising a non-nested control simulation and an analogous nested high-resolution simulation (Table 1). In the first set, referred to as NOBIAS hereafter, the experiments are started from rest and initial ocean temperature and salinity fields are prescribed using the World Ocean Atlas 1998 (WOA98, Levitus (1998)), which includes corrections for the Arctic Ocean by (PHC2.1, Steele et al. (2001)). The benefit here is that both configurations, coarse-resolution ($NOBIAS_C$) and high-resolution nested ($NOBIAS_N$), are allowed to find their own, independent equilibrium state initialised from a state without any biases. On the one hand, this takes full advantage of the finer grid resolution and enables a clear analysis of differences due to the explicit simulation of the

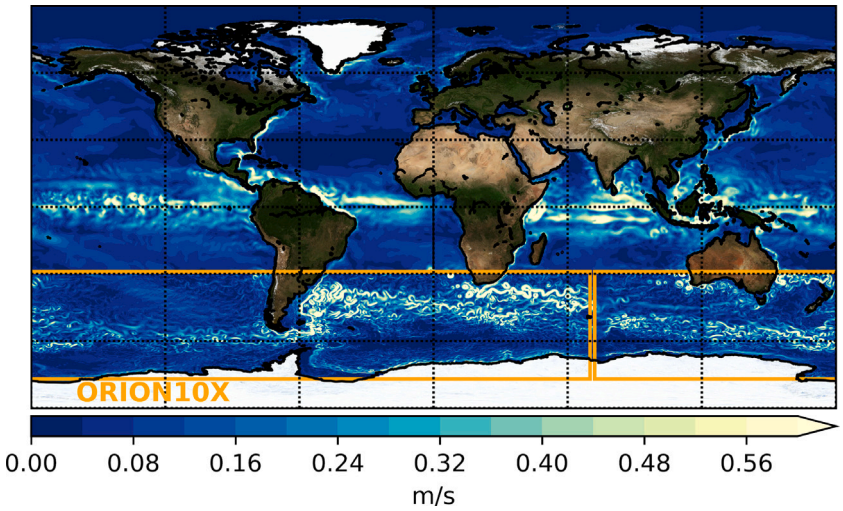

Fig. 1. Snapshot (5-day mean) of near-surface ocean current speed after 200 years of model spin-up. The map highlights the effect of the ORION10X ocean simulation fully coupled by two-way nesting to the global climate model FOCI. The 1/10° grid resolution of the nested domain facilitates an eddy-rich ocean simulation also improving boundary currents such as the Antarctic Slope Current. The extent of the nested domain is marked in orange.

mesoscale (e.g. Martin and Zeller, 0000). On the other hand, a millennial spin-up run similar to the one for the standard FOCI (Matthes et al., 2020) is prohibitive considering the 10-times greater computational costs of FOCI-ORION10X; thus, the ocean, in particular the deep ocean, is not in an equilibrium state after the spin-up period.

We conducted a second set of experiments to take advantage of the spun-up ocean state of FOCI and initialised FOCI-ORION10X, using the state reached after ~1500 years of pre-industrial spin-up. This approach was successfully used by previous studies employing nested FOCI configurations but with grid refinements outside the SO (Ivanciu et al., 2022; Schulzki et al., 2022; Martin and Biastoch, 2023). Unfortunately, this coarse FOCI simulation develops a global ocean temperature bias being particularly strong in the SO (STRONG_C). While the SO temperature deviates by 1.6 °C on average, this is not an uncommon bias for such a model (Wang et al., 2014). Bias build-up is particularly pronounced over the first 800 years and is stronger with greater depth, where it rises above 1.0 °C after 300 and exceeds 1.5° after 500 years (Fig. 2a). From this run we branch off a nested simulation (STRONG_N) after 1520 model years, where we deliberately chose to not start from a state with active open ocean deep convection in the Weddell Sea. This still results in massive deep convection early on in the nested run, discussed further below.

Lastly, seeking a middle ground, we branch off a third nested simulation from an improved FOCI run featuring a significantly reduced warm bias (WEAK_C). The latter employs improvements achieved by the FOCI development team at GEOMAR (Kjellsson et al., 0000), namely increasing the coupling frequency of ocean and atmosphere from once every three hours to hourly and reducing the horizontal eddy diffusivity coefficient `rn_aht_0` from 600 to 300 m^2/s. In addition, we branch off WEAK_N already after 500 years, when the average temperature bias is at only 0.5 °C in FOCI (Fig. 2b), further limiting an impact by the warm bias on the high-resolution simulation.

All three nested experiments ran for 200 years of which the first 100 years are considered a transient period and the second 100 years a quasi-equilibrium period. Overlapping periods from the coarse-resolution control simulations are available for analysis as well and serve as a comparison for the high-resolution simulations. Model output is provided as 5-daily, monthly and yearly averages. Atmosphere, land and sea ice settings are the same in all experiments. Altogether, these six experiments create an exceptional opportunity to (i) provide insight on techniques for initialising a high-resolution nested simulation and (ii) study the implications of SO heat content (or bias) on the representation of major dynamical features in both eddy-parameterised and eddy-rich simulations.

2.3. Representation of mesoscale dynamics

We use eddy kinetic energy ($EKE = \frac{1}{2}\left(u'^2 + v'^2\right)$) as a measure for eddy activity to assess the capability of the high-resolution simulations to model mesoscale dynamics. Here, u' and v' represent the zonal and meridional components of the velocity anomalies. Anomalies are computed as deviations of 5-day mean velocities with respect to the annual average. The simulations exhibit a distinctive pattern of EKE with largest values in the Agulhas region at the southern tip of Africa, in the Malvinas confluence zone east of southern South America and east of Australia near the retroflection of the East Australian current (see Fig. 3a for representative results from NOBIAS_N). A circumpolar zonal band of enhanced EKE between 45–65°S broadly follows the extent of the ACC. High EKE values in the Agulhas region spread in both directions, northwestward outlining the propagation of Agulhas rings and eastward depicting the Agulhas retroflection regime. Both are clear indications of improvements of the nested over the non-nested simulations towards a more realistic representation of the ocean dynamics in this region. A narrow band of enhanced EKE is visible around the coastline of Antarctica indicating enhanced mesoscale activity associated with the Antarctic slope current (ASC), which is well defined in the high-resolution simulations (cf. Fig. 1). The two areas of particularly low EKE depict the interior of the Weddell and Ross gyres where velocity shear is typically small. The EKE patterns are robust across the three nested experiments (not shown) which demonstrates that the representation of mesoscale dynamics in the regions of major currents is independent of the initial SO mean state.

As expected, the non-nested control simulations hardly display any mesoscale activity given that their resolution is too coarse to resolve mesoscale features (not shown). Instead, eddy effects on tracer transport are taken into account using the so-called bolus or eddy-induced velocity (EIV) computed by the GM scheme. In Fig. 3b we provide an impression on where these bolus velocities take effect on surface ocean conditions by displaying half the magnitude of the EIV squared, which yields an equation similar to that of EKE, $|EIV|^2 = \frac{1}{2}\left(u_{EIV}^2 + v_{EIV}^2\right)$ with u_{EIV} and v_{EIV} the bolus-velocity zonal and meridional components. Note, EIV has no direct effect on the momentum budget and acts only on tracer redistribution. Hence, the two maps in Fig. 3 only facilitate a qualitative comparison of eddy active regions. For EIV, we find the Agulhas and Malvinas regions highlighted by larger magnitudes and a zonal band which is shifted to the northern edge of the ACC between 40–50°S (Fig. 3b). Overall, the GM parameterisation adopted in the non-nested simulations compensates for the lack of

Table 1
List of experiments. For nested simulations the horizontal ocean grid resolution in the refinement region is given: 1/10°. Two key parameters differ between the simulations, the coupling time step dt_{cpl} and the horizontal eddy diffusivity $A_{h,l}$ (NEMO namelist parameter `rn_aht_0`). The average temperature bias ΔT_{bias} for the SO (south of 55°S) characterises the three sets of experiments. For control experiments $WEAK_C$ and $STRONG_C$, this is the bias in the branch off year of the corresponding nested simulations. Colour coding corresponds to the colours used in the figures.

Simulation	Grid resolution	Initialisation (branching year)	Length [years]	dt_{cpl} [h]	$A_{h,l}$ [m^2/s]	ΔT_{bias} [°C]	Internal run ID
spin-up	1/2°	WOA98	700	1	300	n/a	FOCI2.0-MZ040
spin-up	1/2°	WOA98	1800	3	600	n/a	FOCI1.3-SW038/-TM020
$NOBIAS_C$	1/2°	WOA98	200	3	600	0.5	FOCI1.3-SW038
$NOBIAS_N$	1/10°	WOA98	200	0.5	120	0.15	FOCI2.0-TM041
$WEAK_C$	1/2°	MZ040 (500)	200	1	300	1.0	FOCI2.0-MZ040
$WEAK_N$	1/10°	MZ040 (500)	200	0.5	60	0.45	FOCI2.0-MZ039
$STRONG_C$	1/2°	SW038 (1520)	200	3	600	1.6	FOCI1.10-TM020
$STRONG_N$	1/10°	SW038 (1520)	200	0.5	60	0.8	FOCI1.25-MZ008

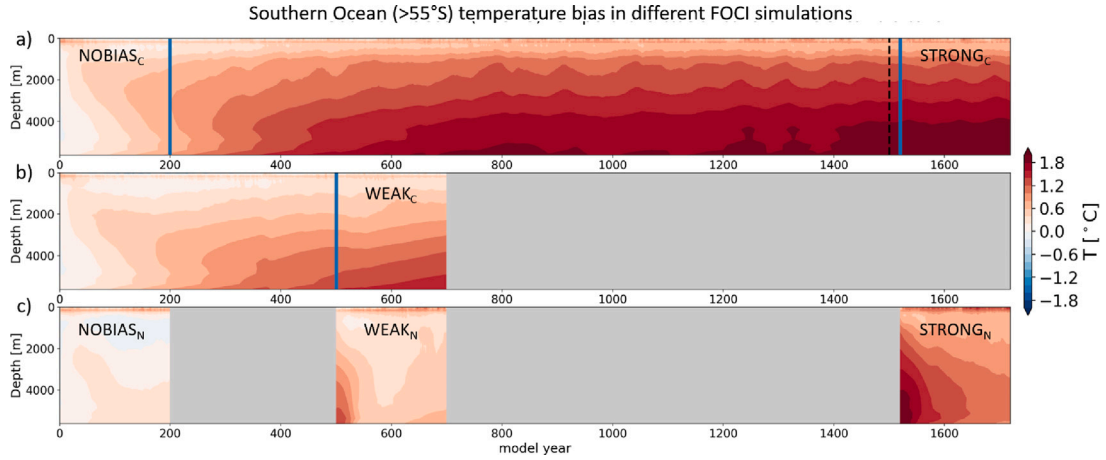

Fig. 2. Southern Ocean temperature bias relative to PHC2.1 data over depth and time for different simulations with FOCI. Panel (a) shows the non-nested simulations $NOBIAS_C$, SW038 (extended by TM020) and $STRONG_C$, panel (b) shows the non-nested simulations MZ040 and $WEAK_C$ with modified mixing parameters and coupling time step, and panel (c) shows the three high-resolution simulations $NOBIAS_N$, $WEAK_N$ and $STRONG_N$, each initialised from different spin-up conditions. The data was average over the Southern Ocean area south of 55°S.

eddies in several key regions but appears to be strongly dampened in the subpolar gyres, under sea ice, and by definition cannot introduce the same spatial and temporal variability simulated at eddy-present grid resolutions.

3. Results

This section is composed of two main parts. The first subsection addresses the consequences of initialising a nested, eddying ocean model from a control simulation with a biased mean state, the corollary of a SO warm bias of different intensity. Besides the temperature distribution, we discuss the bias as driver of open ocean deep convection and the related evolution of large-scale dynamics. In the second part, we compare the mean states (in quasi-equilibrium) of eddying simulations with those of the eddy-parameterised, coarse-resolution counterparts. The analysis covers heat content, the large-scale hydrography of the SO and differences in circulation.

3.1. Nested model initialisation and spin-up

In this section, we investigate the impact of the initial SO mean state on the spin-up of the three high-resolution simulations $NOBIAS_N$, $WEAK_N$, and $STRONG_N$. For the spin-up period, we define the first 100 years of each simulation as this is characterised by obvious drifts in all major ocean quantities. After this period, the majority of the quantities we study here have reached a quasi-steady mean state.

Role of temperature bias

The three initial ocean states have very different temperature distributions in the SO, ranging from unbiased observed conditions (WOA98) in $NOBIAS_N$ to an about 1.6 °C warmer SO originating from $STRONG_C$. We hereby investigate the evolution of the temperature distribution in the high-resolution simulations and, in particular, what role the explicitly simulated mesoscale dynamics play in this.

We begin with sea surface temperature (SST). Although it does not show the most remarkable response, it provides a reference for comparison with other studies. SST averaged over the region south of 55°S is generally higher in the high-resolution simulations initialised from warm biased conditions (Fig. 4a). Both $WEAK_N$ (green line) and $STRONG_N$ (orange) have a positive trend over the 200-years displayed. This is largely a consequence of the warm bias persisting outside the nested domain in these simulations (not only at the surface) and being entrained into the nest across its boundaries. In all three experiments, low-biased sea ice coverage (not shown), particularly in the Weddell Sea and east of the Ross Sea, further adds to the overestimated SST. Aside from lateral entrainment at the surface and missing sea ice, the excessive deep convection in $STRONG_N$ contributes warm SST anomalies. This is due to warmer ocean temperatures at mid-depth in the range of the circumpolar deep water (500–2000 m) compared to surface waters by several degrees.

The temperature bias in the deep ocean below 1000 m evolves differently (Fig. 4b). In $NOBIAS_N$ the accumulation of heat at depth is only marginal and much weaker than in the corresponding control simulation ($NOBIAS_C$), cf. Fig. 2a and c. After 100 years of simulation, the average temperature bias in the deep ocean (below 1000 m)

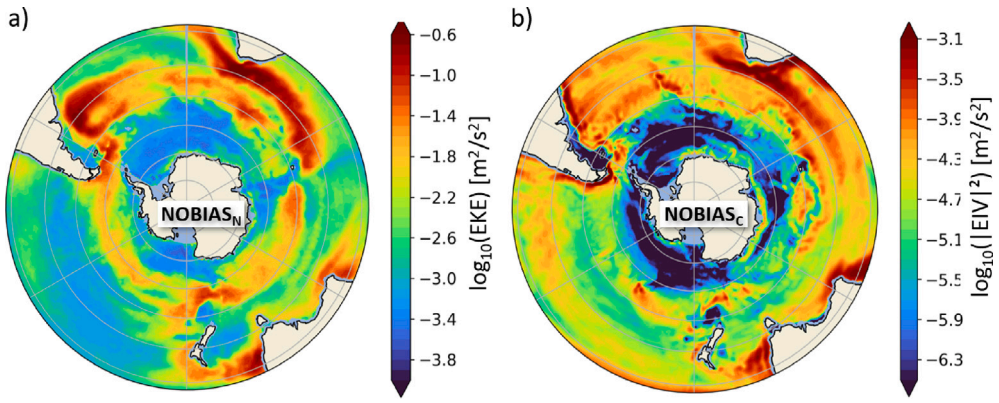

Fig. 3. Spatial distribution of (a) the surface eddy kinetic energy (EKE) in the Southern Ocean simulated with NOBIAS$_N$ and (b) the surface eddy induced velocity (EIV) magnitude from NOBIAS$_C$. EKE is computed from 5-daily mean velocity anomalies referenced to the annual mean. For NOBIAS$_C$ half the squared magnitude of the eddy induced velocity is shown to identify regions where the GM parameterisation takes effect. In both cases, the mean over the final 10 years of each simulation is displayed. Note the different colourbar ranges. The map corresponds to the extent of the Southern Ocean nest.

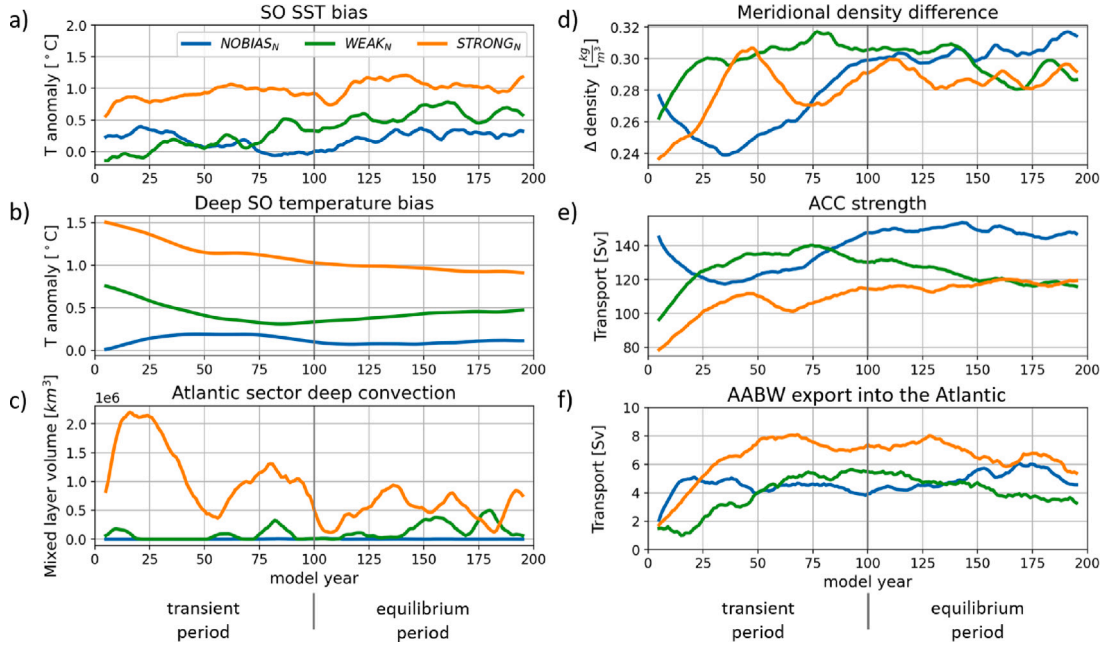

Fig. 4. Time series of major properties and circulation indices of the Southern Ocean (SO), especially the Atlantic sector, from the three high-resolution simulations NOBIAS$_N$ (blue), WEAK$_N$ (green), and STRONG$_N$ (orange). (a) Sea surface temperature (SST) bias averaged over the entire SO south of 55°S, (b) potential temperature bias horizontally averaged for the same region and vertically below 1000 m (see black boxes in Fig. 5), (c) mixed layer volume integrated over the Atlantic sector (55°W–20°E, south of 60°S) of the SO where the local mixed layer is deeper than 500 m, (d) zonally and vertically averaged meridional density difference between 65°S and 45°S, (e) Antarctic circumpolar current strength at Drake passage, and (f) AABW export into the Atlantic as diagnosed from the minimum of the AMOC streamfunction at 30°S. Note that the AMOC minimum was determined for water denser than 36.5 $\frac{\text{kg}}{\text{m}^3}$ in σ_2-space. A 10-year moving average has been applied to all time series.

amounts to only 0.15 °C and remains at this magnitude for the rest of the simulation in NOBIAS$_N$. In contrast, the average deep ocean temperature bias in NOBIAS$_C$ has already increased to 0.44 °C within the same period and keeps increasing. When initialised from a SO with a moderate temperature bias of about 1 °C as present at the beginning of WEAK$_C$, the nested SO immediately acts to remove the bias reducing it to 0.5 °C within only 40 years of integration (WEAK$_N$ in Fig. 2c). Then, the water column appears to remain relatively stable with a comparatively small bias ranging between 0.4°–0.5 °C until the end of the simulation. The bias reduction effect shows up even more pronounced when the nest is initialised from an ocean that is more than 1.6 °C warmer than observed (STRONG$_N$ in Fig. 2c). Within 100 years of the simulation, the temperature bias diminishes to 0.8 °C in the deep ocean. The non-nested SO (STRONG$_C$) in this case has reached its equilibrium state after the long spin-up period and maintains the warm SO conditions. While the temperature bias remains largely stable after the first 100 years until the end of each high-resolution simulation indicating convergence to a balanced state, the three nested SOs approach three different temperature equilibrium states in the range of 0.15°–0.8 °C warmer than today's SO (4b).

Meridional cross sections of the temperature bias (Fig. 5) indicate underlying dynamical processes that are improved in the high-resolution simulations—and those that are not. For the temperature bias itself, we find the heat accumulation in the non-nested simulations to be strongest in the Atlantic sector (70°W–20°E) and concentrated south of 55°S and below 1000 m (Fig. 5a–c). The reduction of the bias during the spin-up of the high-resolution simulations that can already be inferred from Fig. 2, is most pronounced in the Atlantic sector with a decrease averaged over the core bias region ranging between 0.46°–0.65 °C after 100 years (Fig. 5d–f). While a similar pattern is found in the Indian sector (Figure S1) with maxima near the ocean bottom and

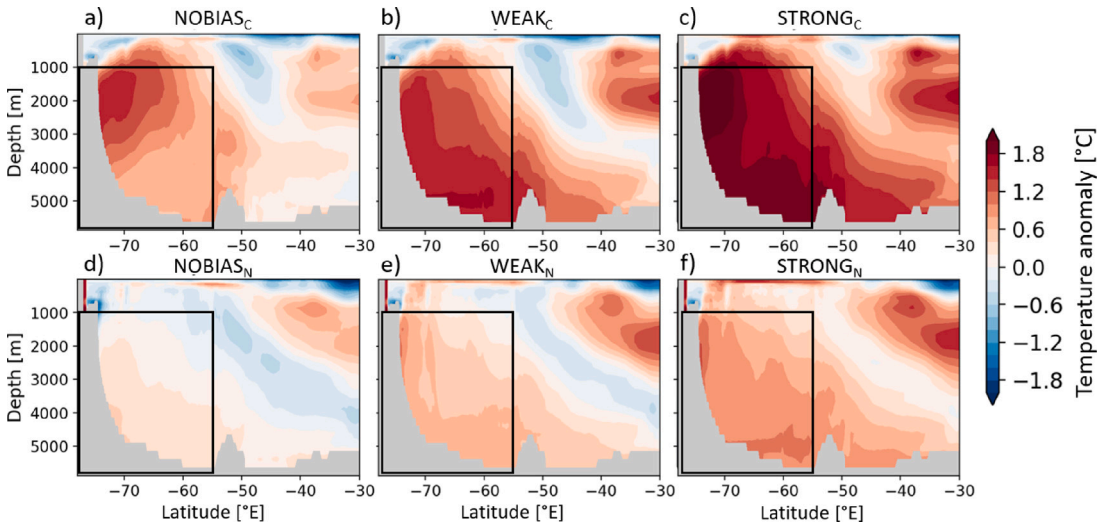

Fig. 5. Temperature bias relative to PHC2.1 data averaged over the Atlantic extent of the Southern Ocean (70°W-20°E). Shown is the mean over the final 100 years of (a) NOBIAS$_C$, (b) WEAK$_C$, (c) STRONG$_C$, (d) NOBIAS$_N$, (e) WEAK$_N$, and (f) STRONG$_N$. The black boxes denote the region of spatial average applied in Fig. 4b.

at the continental slope at 1000–3000 m, the temperature bias in the Pacific (Figure S2) is concentrated on the deep ocean below 3000 m.

We suggest that the strong reduction of the deep ocean temperature bias (below 4000 m) in the nested domain is likely linked to an improved representation of processes on the Antarctic continental shelf (not shown). These processes involve a more realistic representation of dense shelf water production on the Antarctic continental shelf subsequently causing the production of cold and dense Antarctic bottom water to spread into the different ocean basins and thereby reducing the bias. Different ocean dynamics are hypothesised to reduce the temperature bias at intermediate depth (500–4000 m) south of 55°S. Here, the improved representation of subpolar gyre dynamics and the Antarctic slope current in the nested domain are suggested to lead to a decreased accumulation of heat in this region, thus, counteracting the build-up of a bias. On the other hand, we find a tilted dipole structure north of 55°S at approximately 500–2500 m depth in the region of meridional upwelling in all six simulations, indicating a northward displacement of the ocean fronts. The position of the ocean fronts is directly related to the overlying wind field and a consequence of a bias in the position of the westerly winds, which are shifted equatorward in FOCI (Matthes et al., 2020). The decisive role of the atmosphere for this bias in ocean temperature is corroborated by its presence in both coarse-resolution control and high-resolution nested simulations. The wind bias is not improved by introducing eddying resolution to the ocean component.

Impact of deep convection

The accumulation of heat at mid depth in the SO may destabilise the stratification and eventually lead to open ocean deep convection, a process typical for coarse-resolution climate models but rarely observed in reality (Martin et al., 2013). In our non-nested control experiments, the build-up of the warm bias results in periodic occurrences of open ocean deep convection at decadal to centennial time scales first occurring 300–400 years into the spin-up (not shown). In particular, Atlantic sector deep convection events are a recurring feature in STRONG$_C$ branching off the longest spin-up and having the largest heat bias; there is only a single, decade-long event in the spin-up to WEAK$_C$. While absent in WEAK$_C$ itself and also NOBIAS$_C$ and NOBIAS$_N$, we also find open ocean deep convection in the Weddell Sea to occur in high-resolution runs WEAK$_N$ and STRONG$_N$ right from the beginning (Fig. 4c). Obviously, the warm bias inherent to the initialisation fields is not sustainable with only larger eddies explicitly simulated (and eddy parameterisation, i.e. GM, turned off). Here, deep convection first occurs in the south-western Weddell Sea along the path of the Antarctic slope current where both velocity shear and baroclinic instability due to the sharp density gradient between shelf and open ocean creates eddies. However, eddy formation rate and in particular smaller mesoscale eddies are underestimated even at 1/10° grid spacing. In contrast to the coarse resolution simulations, there is no active compensating parameterisation and isopycnals tend to be sloped steeper perpendicular to the shelf in the high-resolution runs compared to their coarse-resolution counterparts. In the latter, the GM parameterisation effectively flattens the isopycnal slopes rising towards the subpolar gyre interior. This is visible in sections through all three SO sectors (Fig. 6d–f, compare black and green contours of isopycnals) as well as in the isotherms of the temperature bias displayed in Fig. 5 (see tilt of white shading near the shelf break above 1000 m). Eventually, the deep convection spreads into the centre of the Weddell Gyre where it is also typically found in the control simulations (not shown).

Deep convection—here indicated by total mixed layer volume at locations of mixed layer depth exceeding 500 m—ceases after two decades in WEAK$_N$ but lasts for 50 years in STRONG$_N$ and recurs quickly for multi-decadal oscillations (Fig. 4c). The "events" in STRONG$_N$ are also characterised by a much greater spatial extent considering that the maximum winter mixed layer depth extends to below 5000 m in both experiments.

Massive open ocean deep convection is the major factor rapidly reducing the deep ocean warm bias in the SO in the two high-resolution simulations that start from a biased state, in particular STRONG$_N$ (Fig. 4b). The onset of deep convection along the southern-most part of the shelf break in the Weddell Sea suggests that sharper fronts due to the finer grid spacing result in enhanced baroclinic instability but—due to a lack of sufficient resolution—cannot trigger sufficient eddy formation and mixing. Instead, vertical mixing is initiated quickly growing out of proportion since warm and salty deep waters are brought to the surface. During periods of deep convection, the ocean below 1000 m loses heat at a mean rate of 0.15 °C/decade while during periods without convection the temperature bias remains largely constant or starts to grow again (Fig. 4b). This result supports the mechanism described in more detail by Martin et al. (2013).

In WEAK$_N$ this is different. We find a cooling trend of the deep SO as strong as in STRONG$_N$ over the first ~80 years (Fig. 4b) though the deep mixed layer volume associated with open ocean deep convection is much smaller (Fig. 4c) only explaining a fraction of the temperature reduction in the circumpolar SO. Instead, WEAK$_N$ starting from an overall weaker warm bias, its ocean state is closer to the equilibrium

state having a more realistic mean hydrography, ACC and gyre circulation than $STRONG_N$. This is similar to $NOBIAS_N$, in which no deep convection occurs at all coinciding with an overall low temperature bias of less than 0.25 °C (Fig. 4b). We can clearly associate these adjustment processes to resolving mesoscale dynamics in the nested, high-resolution runs. Moreover, these simulations also form bottom water on the continental shelf around Antarctica, which takes several decades to fully evolve and helps strengthen the large-scale meridional density gradient (not shown, study in preparation, Martin and Zeller (0000)). Nevertheless, a slight warming trend for the deep SO is visible over the second century of both $NOBIAS_N$ and $WEAK_N$ as the deep ocean evolves towards its individual equilibrium state.

Evolving large-scale circulation

The strength of the ACC strongly depends on the meridional density gradient, typically defined as the difference in zonal mean depth-averaged density between 45°S and 65°S (Beadling et al., 2020). This density difference is sensitive to the presence and subsequent degradation of the warm bias south of 55°S (Fig. 4d). Again, we see the pronounced imprint of the massive deep convection in $STRONG_N$ and smoother transitions to a 15% stronger gradient in $WEAK_N$ and $NOBIAS_N$. The associated adjustment of the ACC in the nested model simulations highly depends on the initial state of the SO (Fig. 4e). When initialised from observed conditions ($NOBIAS_N$), the ACC strength drops from 165 Sv to 120 Sv within the first 25 years of the simulation, then recovers and increases again to almost 150 Sv at the end of the 100-year spin-up period, which is roughly in accordance with observed estimates (Koenig et al., 2014; Donohue et al., 2016; Vargas-Alema et al., 2023). Though the model evidently struggles to support the observed hydrography, proper AABW formation through processes on the continental shelf and its export at depth is established within a few decades (not shown). The quasi-equilibrium at the end of $NOBIAS_N$ shows that the nested configuration supports an ACC strength in the range of 140–160 Sv simulated by comparable climate models (Beadling et al., 2020), which is just in the range of the very recent observational estimate of 149 Sv (Vargas-Alema et al., 2023). The ACC in the other two high-resolution simulations starts from very low values of <80 Sv and 90 Sv inherited from the control runs $WEAK_C$ and $STRONG_C$, respectively. Still, mitigating the SO warm bias enables the ACC strength to rise by about 1 Sv/yr on average in the first 40–50 years in both simulations reaching 115 Sv ($STRONG_N$) and 135 Sv ($WEAK_N$).

The imprint of deep convection on the meridional density difference is clearly visible in $STRONG_N$ (orange lines in Fig. 4c and d). The two time series correlate with a maximum lagged coefficient of 0.64 reflecting an increase in the meridional density difference while heat is released from the deep SO south of the ACC to the atmosphere. Since the meridional density difference directly imprints on the ACC through thermal wind balance, the effect of the strong deep convection is also visible in the ACC strength time series (orange lines in Fig. 4c and e), where the current is particularly strong during periods of enhanced deep convection. The imprint is less obvious for $WEAK_N$, in which ACC strength rather declines over the second century of the experiment. This supports our earlier statement that deep convection plays a minor role in setting the equilibrium state of $WEAK_N$ in contrast to $STRONG_N$. After 100 years of the simulation, we find the three nested experiments stagger in ACC strength according to the intensity of the initial temperature bias with $NOBIAS_N$ having the strongest and $STRONG_N$ the weakest ACC. Over the next 100 years, however, $WEAK_N$ converges toward the weaker state and both simulations suffering from a biased initialisation cannot reach the same strength as $NOBIAS_N$. We speculate that this difference is likely related to biases that have evolved outside the SO and cannot be mitigated by improved dynamics directly in the nested domain.

Processes in the SO also affect the ocean circulation outside the nested domain. Most importantly, the SO contributes to the upper and lower branches of the meridional overturning circulation (MOC) as demonstrated by Toggweiler and Samuels (1998), Kamenkovich and Sarachik (2004), and Nikurashin and Vallis (2012). Notably, the lower MOC cell is an indicator for the export of AABW towards lower latitudes. In most climate models, the formation of AABW is strongly related to open ocean deep convection, where AABW export constitutes a time-lagged integral of SO deep convection. In FOCI, deep convection and AABW export is concentrated in the Atlantic sector and we thus show the strength of the deep northward flow of the Atlantic meridional overturning circulation (AMOC) at 30°S as a measure of AABW volume export in Fig. 4f. As expected, the two large deep convection events during the transient period of $STRONG_N$ (Fig. 4c) are accompanied by a continuous increase in AABW export (Fig. 4f). In $WEAK_N$, AABW formation changes from open ocean deep convection–driven to on-shelf production, the associated export increases at a reduced rate, and the strength of the deep AMOC cell cannot directly be related to the weak convection events still present in this experiment. After a rapid increase within the first 15 years, AABW export in $NOBIAS_N$ stays at a relatively constant level of 4–6 Sv which underestimates observed estimates of ~8 Sv (Orsi et al., 1999; Zhou et al., 2023) but is at the higher end of the range simulated by comparable climate models (Heuze, 2021, Atlantic SMOC in their Tab. B2).

In conclusion, both $WEAK_N$ and $STRONG_N$ can substantially reduce the excess heat content of the sub-surface and deep SO during the first 100 years, which these runs were initialised with (Figs. 2 and 5). Nonetheless, these two simulations perform less than $NOBIAS_N$ with the least biased ocean state, featuring the most realistic SO hydrography. $STRONG_N$ is further adversely affected by the unrealistically strong deep convection (Fig. 4c), which to the disadvantage of this run is reflected in the deep ocean, for instance, as a prominent signal in AABW export and AMOC strength.

3.2. Differences in mean states

In this section we discuss the quasi-equilibrium mean states of both the control and the eddying simulations now averaging over the second 100-year period of each of the six simulations (see Table 1). Effects of resolution are analysed based on the differences between coarse and high-resolution runs, while the potential imprint of the warm bias based on differences of runs of same resolution. The focus is on differing SO heat content, implications for hydrography and resulting variations in large-scale dynamics. In the following, $NOBIAS_C$ and $NOBIAS_N$ will serve as "ideal" cases featuring the smallest biases. Both the "ideal" reference cases and the quasi-equilibrium are relatively strong assumptions that allow us to stay within the framework of the available simulations. Changes in ocean dynamics are manifold and complex, and the analysis here can only provide an overview of the most prominent effects connecting large-scale circulation and hydrography. These differences also have implications outside the SO and may help interpret other climate model results.

Heat distribution

To demonstrate the effect of resolved mesoscale activity on the state of the SO, we first examine the differences in heat content between the eddy-parameterised and eddying simulations. A map of vertically integrated total heat content in Fig. 6a shows a significantly lower heat content in the eddying runs in the Atlantic basin and in a circumpolar band south of 60°–70°S and greater content everywhere else in the SO with distinct maxima in the Malvinas and Agulhas regions. The pronounced dipole just south of the African continent—warming of the Agulhas retroflection region towards the Indian sector and cooling in region of leakage into the South Atlantic—clearly highlights the effect of enhanced mesoscale activity in this area in the nested experiments (cf. Fig. 3). The cooling at the western flank in the high-resolution simulation originates from a more realistic turbulent flow around Cape of Good Hope with transient eddies transporting heat into the Atlantic

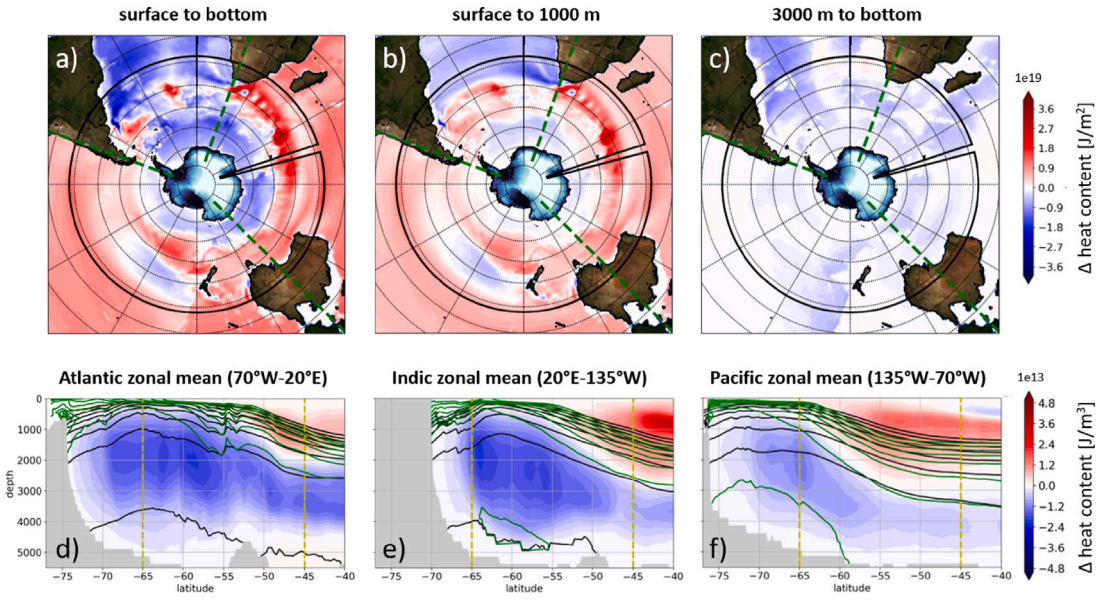

Fig. 6. Long-term mean difference of $NOBIAS_N$ minus $NOBIAS_C$ of the vertically (a–c) or zonally (d–f) integrated heat content. Heat content difference for (a) the entire water column, (b) the upper 1000 m, (c) the water column below 3000 m, (d) across the Atlantic sector, (e) across the Indic sector, and (f) across the Pacific sectors. Red (blue) indicates regions with larger (smaller) heat content in the nested simulation. Averages over the final 100 years of the simulations are displayed. The black circle in (a–c) depicts the extent of the SO nest, grid resolution is 1/10° within and 1/2° outside. The green dashed lines in (a–c) mark the longitudes used to define the three ocean basins shown in (d–f). Average heat content in (d–f) has been normalised by the zonal extent of each basin. The black (green) contours show the mean isopycnals of $NOBIAS_C$ ($NOBIAS_N$). The yellow dashed lines mark the latitudes used for computing the meridional density difference.

Ocean. The non-eddying experiments, instead, simulate a direct near-laminar flow around the tip of South Africa from the Indian into the Atlantic basin. This flow causes an unrealistically large heat transport into the Atlantic as seen by the blue shading in the difference plot (Fig. 6a and b). The improved representation of mesoscale features in this region also provokes an enhanced retroflection of the Agulhas current in the eddying simulations due to a reduced, eddy-driven leakage, while in the coarse-resolution simulations the retroflection is weaker from the comparatively large near-laminar flow into the Atlantic. Hence, the eastward heat transport is larger in the high-resolution simulations (red shading east of South Africa in Fig. 6a and b). This increased heat transport is incorporated into the ACC and the subtropical supergyre resulting in an increased heat content throughout the entire Indian Sector and part of the western Pacific. The reduced heat leakage into the Atlantic decreases the upper ocean heat content in the Atlantic and enhances it in the Indian and Pacific basins with the integral above 1000 m explaining a large part of the difference (Fig. 6b).

Overall, greater heat content in the nested runs is confined to above 2000 m and north of approx. 55°S in all three sectors of the SO, practically in and above the density range of deep water (6d–f). In contrast, the southern hemisphere deep mid- to high-latitude ocean has less heat content in the high-resolution simulation than in the coarse resolution run (Fig. 6c) reflecting the build-up of the warm bias in the latter and also demonstrates the preference of the deep ocean to warm more strongly. We attribute this improvement to the more realistic formation of Antarctic bottom water (AABW) on the continental shelf and its enhanced export in the high-resolution simulation (cf. Fig. 4f). The pattern of reduced deep ocean heat content is consistent with the circumpolar distribution of AABW and the typical export routes guided by bathymetry, e.g., along the Antarctic peninsula into the western South Atlantic basin and similarly along the western shelf boundaries of the Pacific and Indian basins (Fig. 6c).

The meridional transects through the SO show a cooling around Antarctica being centred between 55°–65°S and 1000–3000 m (Fig. 6d–f). Further, the heat content reduction is strongest in the Atlantic and Indian sectors clearly indicating changes in circumpolar deep water import and heat accumulation in the Weddell Gyre, associated with the explicit simulation of mesoscale dynamics.

The increased heat content in the upper ocean north of 45°S is a consequence of the improved Agulhas retroflection in the nested experiments, which enables greater heat advection eastward. This is seen most prominently in the Indian sector while it can be tracked further into the Pacific sector as well (between 150°–180°W), with the warming shifted southward by about 10° (Fig. 6b,e and f). This large-scale transport is likely related to the so-called southern hemisphere supergyre which spans the entire SO in a circumpolar gyre circulation comprising the southern branches of the three subtropical gyres of the Atlantic, Indian and Pacific basins (Speich et al., 2007). Originating from the stronger Agulhas retroflection, an associated greater heat content could connect to the Pacific basin. The local warm heat content anomaly in the western Pacific is confined by bathymetry and aligns with the Antarctic-Pacific mid-ocean ridge.

In the simulations starting from a warmer SO, $WEAK_N$ and $STRONG_N$, the patterns of heat content difference due to resolving the mesoscale are very similar (Figures S3-S4). However, the cooling effect on the deep ocean is markedly stronger in $STRONG_N$ than in the other two simulations. Both runs start with a significant warm bias. Particularly in $STRONG_N$ massive open ocean deep convection results in basin-scale heat loss of the mid to deep ocean below 1000 m. Introducing mesoscale dynamics also leads to a horizontal redistribution of heat and an adjustment of ocean fronts in the SO. This results in an enhanced heat content in the high-resolution simulations with respect to their control counterparts in the upper ocean above 1000 m, which is also more pronounced in $WEAK_N$ and $STRONG_N$ compared to $NOBIAS_N$.

In the broad scheme of total SO heat content, explicitly simulating eddies instead of parameterising their effect has an ameliorative effect that is to first order rather similar for all three initialisation scenarios. The left column in Fig. 7a shows deviations from the total SO heat content of $NOBIAS_C$ for the two biased control runs (circles) and also for the three nested experiments (stars). The stronger the warm bias, the more positive the heat content deviation. This still applies to the nested experiments inheriting no, a weak or strong bias despite the improvements achieved by simulating mesoscale dynamics. In fact, the

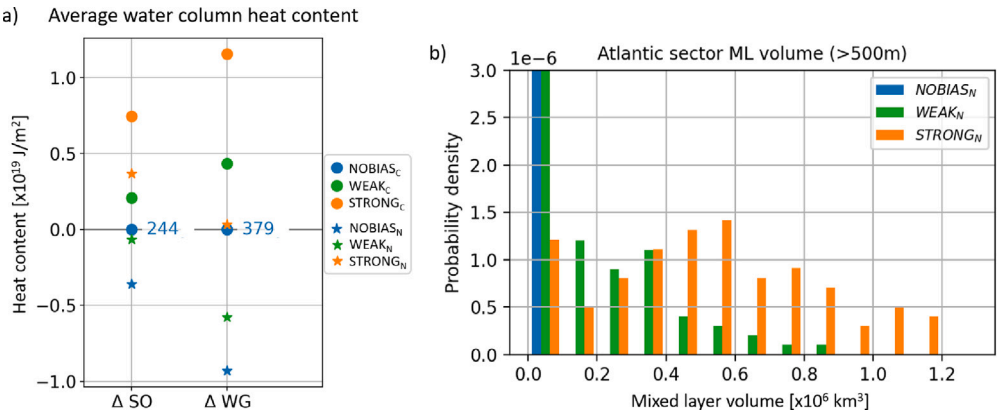

Fig. 7. (a) Quasi-equilibrium Southern Ocean (SO) and Weddell Gyre (WG) heat content vertically and zonally averaged (mean over model years 101–200) displayed as deviation from $NOBIAS_C$ for all experiments. Control simulations are depicted by filled circles, nested ones by stars. Different colours correspond to the different SO warm bias states. The absolute values for $NOBIAS_C$ are displayed in blue for reference. We define the SO as the ocean south of 55°S and limit the WG to the boundaries 55°–65°S and 50°W–50°E. (b) Histogram of mixed layer volume integrated over the Atlantic sector (60°W-20°E, south of 55°S) of the SO where the local mixed layer is deeper than 500 m for the final 100 years of $NOBIAS_N$ (blue), $WEAK_N$ (green), and $STRONG_N$ (orange).

heat reduction is to first order rather similar (compare distance between circles and stars). The effect appears a bit smaller for $WEAK_N$, which can be explained by a warming tendency in the deep SO over the second century of the experiment (cf. Fig. 4b).

The Atlantic sector with the Weddell Gyre plays a prominent role in the evolution of the warm bias in the control runs and hence also for the reduction of the bias in the nested experiments. Here, the effect of mesoscale dynamics is even more striking (Fig. 7a, right column). The Weddell Gyre holds considerably less heat in the high-resolution simulations and the heat content of $STRONG_N$ becomes comparable to that in $NOBIAS_C$. A closer look reveals that the cooling of the Weddell Gyre in the high-resolution simulations grows with an increasing mean heat content in the control simulation, ranging from 0.8×10^4 PJ in $NOBIAS_N$ to about 1.0×10^4 PJ in $WEAK_N$ to 1.2×10^4 PJ in $STRONG_N$. This is related to enhanced deep convection activity triggered by a warming deep ocean. While there is no deep convection occurring in $NOBIAS_N$ it is present in both $WEAK_N$ and $STRONG_N$, but with greater probability for larger mixed layer volumes in $STRONG_N$ (Fig. 7b). This can be attributed to a widely less stably stratified WG caused by the accumulation of warm deep water originating from outside the nested domain and carrying the major warm bias of $STRONG_C$. This agrees well with the overall impression that introducing mesoscale dynamics does not importantly change the offset between experiments of same grid resolution. The initial warm bias—though diminished—maintains an impact on large-scale SO conditions (order of and distance between stars compared to that between circles).

Hydrography

The redistribution of heat in the high-resolution simulations has a direct effect on the density structure of the SO. The water column below 500 m is on average 0.5 °C cooler in the nested than in the non-nested experiments (not shown); thus, relatively dense water reaches the upper ocean (above 200 m) and resides closer below the mixed layer south of 65°S. As a consequence, the isopycnal slope between 45° and 65°S is considerably steeper in the nested experiments in all SO sectors (Fig. 6d–f, black and green contours). In the following, we describe the implication of such differences in density on the meridional gradient that drives the ACC and how the density differences are related to changes in temperature and salinity. We quantify the differences by computing zonally and vertically averaged meridional differences in density, temperature and salinity between 65°S and 45°S. The time-mean changes are then referenced against $NOBIAS_C$ to quantify the effect of a warm bias ($WEAK_C$ and $STRONG_C$) and of explicitly simulating mesoscale eddies (nested experiments).

In Fig. 8, we present the density gradient differences in the same framework as the heat content deviations before (cf. Fig. 7). We expect a warm bias in the SO (<55°S) to reduce the density gradient across the ACC as the temperature discrepancy to the mid latitudes is diminished, i.e. $\Delta\rho$ is lower in WEAK experiments and even lower in the STRONG ones and the effect is smaller in the nested runs since the warm bias has been reduced. The picture drawn in Fig. 8(left panel) is not that clear, however. While $STRONG_C$ (orange circle) does present a negative $\Delta\rho$ deviation from $NOBIAS_C$ (blue circle) as expected, in $WEAK_C$ (green circle) the density difference is slightly larger. We attribute this unexpected behaviour to the reduced warm bias achieved through improved parameter settings in $WEAK_C$ causing this run to have a stronger ACC after 500 years than $NOBIAS_S$ after only 200 (not shown). The high-resolution simulations (stars) have significantly enhanced $\Delta\rho$ compared to the control runs; moreover, $NOBIAS_N$ has the greatest density difference to $NOBIAS_C$ and $STRONG_N$ the smallest, which matches our expectations and also goes in line with the ACC strength shown in Fig. 4d. Interestingly, the differences in $\Delta\rho$ between the nested runs are larger (or of opposite sign) than those between the control runs. We thus take a closer look at the role of the meridional temperature and salinity differences in setting the density gradient.

Temperature clearly plays the dominant role determining the density difference in the control runs. We find the same order for ΔT as for $\Delta\rho$ (cf. circles in Fig. 8, left and middle panel) suggesting a direct relationship between the two variables. In contrast, salinity (circles in right panel) shows a different order with $WEAK_C$ in between $NOBIAS_C$ and $STRONG_C$, i.e. the high latitude warm bias is associated with a positive salinity bias following the accumulation of circumpolar deep water at depth. We conclude that the warm bias dominates the density difference and hence ACC strength in the control runs. This demonstrates the important effect of a SO warm bias on ACC dynamics by simple thermal wind balance, which holds beyond our simulations.

For the high-resolution simulations we find that the salinity difference across the ACC deviates little from the control state in $WEAK_N$ and $STRONG_N$. The exception is $NOBIAS_N$, which is not influenced by any coarse-resolution model bias and features a major positive deviation from $NOBIAS_C$ indicating that the meridional salinity gradient is vastly underestimated in all the other simulations to the disadvantage of ACC strength. In $NOBIAS_N$ this helps to create a stronger density difference compared to $WEAK_N$ (left panel) despite both simulations having equal meridional temperature gradients (middle panel, green star on top of blue star).

To illustrate the impact of the temperature bias on either side of the ACC, polar vs. mid latitudes, we additionally present the temperature deviations from $NOBIAS_C$ for the latitude bands of 65°S and 45°S

(Fig. 8, middle panel). Such direct temperature comparison yields the sequence we originally expected, orange symbols on top of green on top of blue, i.e. conditions are warmer in WEAK than in NOBIAS and again warmer in STRONG simulations. This holds for both control (circles) and nested runs (stars) as well as for 65°S and 45°S latitude. If the same symbol appears at a greater temperature deviation from NOBIAS_C at 45°S than at 65°S, ΔT will be positive, and so will be $\Delta\rho$. This is the case for all simulations except for STRONG_C (orange circle), which in consequence yields a negative ΔT. From this we take away that (i) all simulations including NOBIAS_N have a stronger warm bias north of the ACC than NOBIAS_C with the nested versions exceeding their non-eddying counterparts (see discussion of Fig. 6a,b), (ii) implementing the SO nest with eddying resolution south of 28°S yields major warm bias relief south of the ACC, and (iii) greater ΔT and $\Delta\rho$ in the nested runs are a consequence of both a reduced warm bias on the cold, southern side of the ACC and an enhanced bias on its warm, northern side. The effect at polar latitudes is three times stronger in NOBIAS_N and STRONG_N whereas of comparable magnitude in WEAK_N (offsets between stars and circles of same colour and latitude).

Dynamics

The strong meridional density gradient and associated greater baroclinicity in the high-resolution simulations triggers the formation of mesoscale eddies. Accordingly, EKE is enhanced in the latitude band between 50°S to 65°S in the eddying simulations. The relationship is best demonstrated for a Pacific sector cross-section of NOBIAS_N (Fig. 9a). In the Atlantic sector, the enhanced EKE of the Malvinas confluence and the Agulhas regime north of the ACC diminishes the prominence of the EKE band associated with the steep isopycnals in the upwelling region, even on circumpolar average (cf. Figure S5). EKE is strongest at mid latitudes above 1000 m. We also find a bottom layer of enhanced EKE below 5000 m along topography. At polar latitudes surface-intensified EKE is confined to the top 200 m. In the interior, deep ocean between 1500 and 4000 m EKE is typically low. However, the circumpolar wind-driven upwelling between 50°S and 65°S forces isopycnal sloping causing enhanced EKE throughout the entire water column. In particular, the maximum EKE below the core of the ACC at ~1500–2000 m depth is in line with the enhanced eddy mixing related to locally enhanced baroclinicity over topography as described by Marshall et al. (2006) and Lu and Speer (2010). In contrast, the eddy induced velocities by the GM parameterisation in the non-eddying control simulations exhibit a fundamentally different vertical structure. A cross-section of $|EIV|^2$ in NOBIAS_C highlights areas of particularly active GM (Fig. 9b). We do not find a pronounced band of enhanced $|EIV|^2$ associated with the isopycnal slopes but enhanced magnitudes in the upper ocean down to 300 m and topography-induced $|EIV|^2$ reaching higher up to about 2500 m, affecting the lower half of the interior ocean. Importantly, the smaller meridional density gradient—with respect to the high-resolution simulations—does not invoke the presence of high GM activity at mid-depth between 500 m and 2500 m. In particular, $|EIV|^2$ is minimal in the centres of the subpolar gyres, here the Ross gyre, at 500–2000 m depth between 58° and 70°S (cf. Fig. 3).

As laid out in the previous Section 3.1, thermal wind balance links the meridional density gradient with the large-scale circulation in the SO. This relationship not only affects the dynamics during transient periods but also determines the mean state of the simulations (Fig. 10). We find a stronger ACC with reduced temperature bias and stronger density gradient, as reported above. The very clear order of the symbols for the control (circles) and nested runs (stars), which slightly divert from those of $\Delta\rho$ and ΔT in Fig. 8, shows that ACC transport is defined by other processes as well. In contrast, both Weddell (WG) and Ross gyres (RG) are weaker in the high-resolution simulations compared to the corresponding control runs (Fig. 10). In fact, there is a distinct anti-phase relationship between the ACC and the subpolar gyre strengths on interannual to decadal time scales (not shown): a strong ACC coincides with weak subpolar gyres and vice versa. The long-term mean states in Fig. 10 only show this for ΔWG of the nested runs (stars). Ross gyre strength rather forms two clusters with a difference of about 10 Sv allowing no clear conclusions to be drawn from.

The Agulhas current (AC), the most prominent feature at mid latitudes, strengthens by ~12% in the high-resolution simulations (9–13 Sv increase compared to a 89 Sv mean in NOBIAS_C, Fig. 10). We compute the Agulhas current from the barotropic streamfunction at the Agulhas current repeat transect ACT. Nevertheless, leakage into the Atlantic is reduced in the nested runs by turning this exchange from direct flow into a realistic eddy shedding process. Both, enhanced AC and reduced eddy shedding, lead to an increased eastward heat transport. This is in line with the increased heat content in the upper 1000 m of the Indo-Pacific basin apparent in the high-resolution simulations (cf. Fig. 6b). Regarding changes in AC strength due to the different warm biases, the control simulations show close to no change (circles for ΔAC in Fig. 10). There is a tendency for a stronger AC with a warm-biased SO in the high-resolution simulations (stars for ΔAC in Fig. 10), which is potentially linked to a weaker ACC under warmer conditions.

4. Discussion

We investigated consequences of a warm biased SO in global climate model simulations of coarse, non-eddying and high, eddying grid resolution on the initialisation of nested simulations and on the quasi-equilibrium of SO properties. While this study discusses the behaviour of simulations with different warm biases, some of the described processes and mechanisms may also hold under global warming as recently outlined by Ferster et al. (2019). In the first part, the focus is on the implications of varying amounts of heat in the deep SO for the initialisation and subsequent spin-up phase of a high-resolution SO nest. Our experiments show that a warm bias in the initial state inherited from a coarse-resolution model spin-up causes the high-resolution model to be dynamically unstable. The majority of the excess heat is depleted by deep convection causing massive heat loss to the atmosphere. In our experiments, this happens predominantly in the Atlantic sector of the SO where heat accumulation is strongest in all our model simulations. The mechanism driving the open ocean deep convection was described in detail by Martin et al. (2013) based on a previous version of the present model. Dufour et al. (2017) showed that a stronger upper ocean stratification in a high-resolution simulation (1/10°) can favour heat build-up at depth and deep convection events in contrast to an eddy-parameterised simulation (1/4°) with continuously stronger vertical mixing. Our simulations indicate that coarse-resolution configurations tend to accumulate heat at depth over time due to misrepresented dynamics. Vertical mixing parameterisation and periodic deep convection activity ultimately do not inhibit heat accumulation in the deep ocean though parameterisations can affect the frequency and intensity of the deep convection (Heuze et al., 2015; Kjellsson et al., 2015). A possible explanation for the discrepancy with Dufour et al. (2017) might be a too strong GM parameterisation in the present coarse-resolution model configuration causing excessive restratification and therefore allowing heat to accumulate at depth.

The accumulation of heat at depth in turn effects an overall weakening of the stratification, which is a necessary precondition of deep convection events. Such an effect has also been observed by Zhang et al. (2021) who analysed repeated ship-based hydrographic surveys. They further relate the modified stratification under warmer conditions to changes in heat flux and internal wave generation and dissipation eventually imprinting on the strength of the abyssal MOC. Similarly, Tan and Thurnherr (2023) report an observed reduction in stratification in the SO during recent decades and associate this with changes in AABW properties. They suggest that these changes are spread across the abyssal ocean along AABW export pathways also affecting adjacent ocean basins.

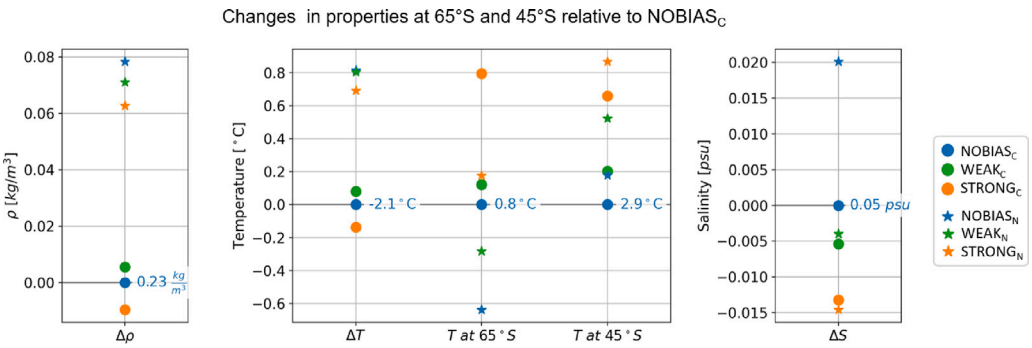

Fig. 8. Time-mean SO water properties zonally and vertically averaged and displayed as deviations from NOBIAS$_C$ for all experiments. The left panel shows the meridional density difference $\Delta\rho$ between 65°S and 45°S, the middle panel shows the temperature difference ΔT between 65°S and 45°S as well as temperatures T at the respective latitudes, and the right panel shows the salinity difference ΔS between 65°S and 45°S. Control (nested) simulations are indicated as filled circles (stars). Different colours correspond to the different SO warm bias states. The absolute values for NOBIAS$_C$ are displayed in blue for reference.

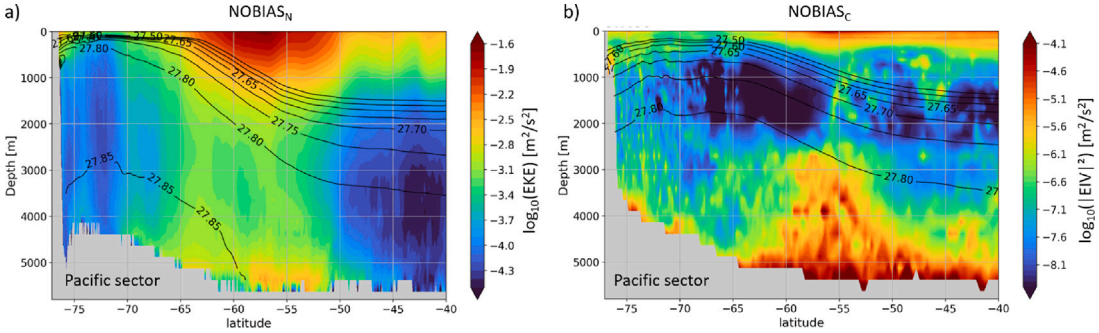

Fig. 9. Pacific sector (135°E–70°W) zonal mean section of potential density (black contours) and EKE/$|EIV|^2$ (shading) of (a) NOBIAS$_N$ and (b) NOBIAS$_C$. All data has been averaged over the final 10 years matching the EKE/$|EIV|^2$ maps in Fig. 3. Note the different colourbar ranges.

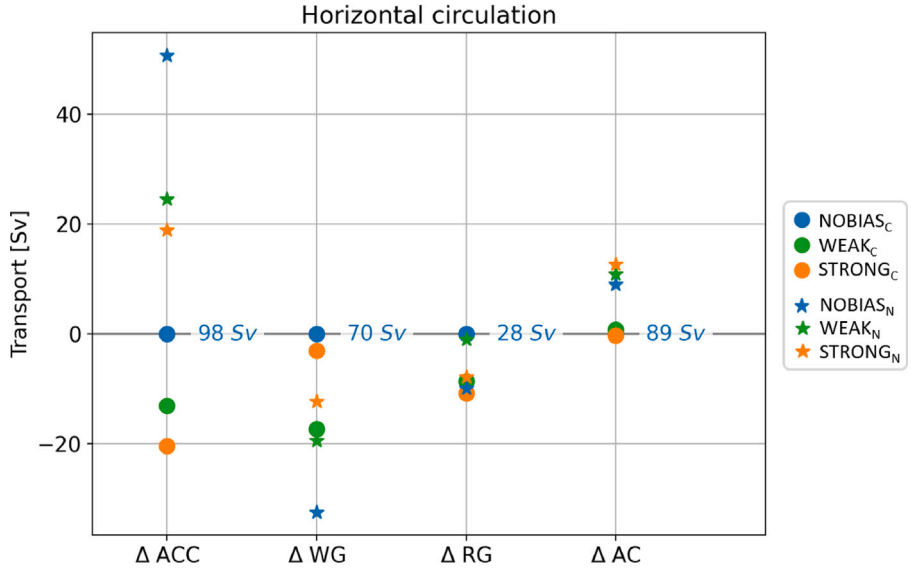

Fig. 10. Differences of mean SO circulation features relative to NOBIAS$_C$ for all experiments. From left to right the columns depict volume transport deviations for the Antarctic circumpolar current (ΔACC), the Weddell Gyre (ΔWG), the Ross Gyre (ΔRG), and the Agulhas current (ΔAC). Control (nested) simulations are indicated as filled circles (stars). Different colours correspond to the different SO warm bias states. The absolute values for NOBIAS$_C$ are displayed in blue for reference.

In our simulations with strong SO warming, i.e. a well expressed warm bias, open ocean deep convection is the main relief mechanism. As we show, this has direct implications for the hydrography at high latitudes and imprints on the large scale circulation of the SO, not only the ACC but also the subpolar gyres, the Agulhas current and ultimately the export of AABW and thus the MOC. This is different from, for instance, a bias in surface winds. Morrison and Hogg (2013) do not find wind stress changes affecting the ACC to also imprint on the MOC. Changes in Southern hemisphere surface wind speeds may still also act as a driver for changes in SO heat content and surface temperatures as shown by Ferster et al. (2019).

If instead the SO nest is initialised from observed conditions, no comparable warm bias forms and the model slowly adjusts to its own mean state that is truly superior to that of the coarse-resolution

simulations. Only this approach takes full advantage of the eddy-rich dynamics of the high-resolution model configuration. We conclude that an inherited, strong bias in an initial SO state thus may have long-lasting implications for the climate state in coupled model simulations. This is in line with Singh et al. (2023) who find in a large ensemble simulation of the Canadian Earth system model (CanESM2) a persistent anomaly in the SO surface climate and attribute this to varying ocean initial conditions.

The second part of the present study sheds light on how the SO mean state is affected by different amounts of SO heat in spun-up climate simulations at eddying and non-eddying ocean resolution. At this point, it should be noted that—in an ideal case—the two high-resolution experiments STRONG_N and WEAK_N should eventually converge to the same equilibrium state, as they only differ in their initial condition and in the diffusivity applied outside of the nested domain. Consequently, the differences that are discussed with respect to their mean states (see Section 3.2) are not due to inherently different dynamics but rather reflect the fact that, even after 100 model years, the two simulations have not yet reached their equilibrium state. While some mechanisms are rather unaffected by the mean state and scale with the bias other relationships break down. The relationship between deep convection and SO circulation in our simulations is consistent with the results of Behrens et al. (2016). They show a decrease of the subpolar gyre strength and an increase of the ACC strength with increased deep convection activity on decadal to multidecadal time scales in a multi-model ensemble based on CMIP5. The anti-phase relationship between the ACC and the subpolar gyre found in all simulations could be a consequence of the varying area of the subpolar gyres. As shown by Meijers et al. (2012), the position of the northern edge of the Weddell and Ross gyres is critical to the net ACC transport, i.e., a larger (smaller) subpolar gyre area is associated with a weaker (stronger) ACC transport. The variability might result from large-scale climate variations like the Southern annular mode, as suggested by Liau and Chao (2017). The consistent response of the two gyres (WG and RG) to a change in SO heat content supports the conception of a SO supergyre connecting multiple sub-gyres spanning the Weddell and Ross seas as proposed by Sonnewald et al. (2023) based on physics-informed machine learning. Hence, we can conclude that the mechanism itself works independent of model type and initial state but we must acknowledge that the mean state itself is dependent on the initial conditions irrespective of the model configuration.

Yet, we also find consistent improvements with the higher spatial resolution in the nested configurations independent of the initial state meaning that the effect of explicitly simulating eddies is greater than the consequences of the warm bias. This is, for instance, true for the Agulhas leakage where in eddying simulations the dynamics shift from a direct flow to eddy shedding which facilitates a realistic eddy-driven transport of heat into the Atlantic and results in a much more realistic Atlantic SST and regional heat content. Moreover, the mean strengths of the Agulhas and Drake Passage volume transports do compare considerably better with observations in eddying simulations. Another example for a dynamical shift towards a more realistic SO is the relocation of major deep convection sites from the open ocean, as is the case in coarse-resolution simulations, to shelf regions in eddying simulations. A very similar shift of deep convection sites was found by Ma et al. (2020) who attribute the changes to the turning angle between sea ice and ocean velocity in a coarse-resolution climate model. Our results show that even with an identical parameterisation of the sea ice–ocean horizontal momentum exchange a more realistic representation of SO deep convection can be achieved by facilitating mesoscale dynamics with an increased ocean model resolution.

The most realistic results are obtained with the eddying simulation initialised with an observation-based ocean state. For example, the mean ACC strength improves from 80 Sv to 149 Sv as compared to the most recently observed values of 149 Sv (Vargas-Alema et al., 2023), 141 Sv (Koenig et al., 2014) and 173 Sv (Donohue et al., 2016). This is also in agreement with the 157 Sv of Xu et al. (2020) who based their analysis on a 1/12° global ocean model. The mean Weddell gyre strength also improves from 70 Sv to 50 Sv as compared to observed values of 50 Sv (Klatt et al., 2005; Vernet et al., 2019). The eddying simulations initialised with a biased ocean state do not reach a similar quality.

5. Conclusion

We draw two main conclusions from the analysis and discussion presented here. Firstly, the stratification of the SO is highly sensitive to the dynamics either resolved by or parameterised in the model. The ocean heat content plays a major role both affecting the stratification as well as being set by processes influencing buoyancy, such as surface fluxes. SO heat content is strongly connected with the large-scale circulation as it sets the meridional density gradient determining ACC strength and is governed by upwelling of deep water and its import into the subpolar gyres. We demonstrated that a SO warm bias characteristic of non-eddying climate models may not be sustained by a similar but strongly eddying model configuration. Thus, initialising a high-resolution nested simulation from a mean state of a different model may lead to spurious dynamical behaviour in the high-resolution simulations regarding stratification, stability, deep convection, overturning and gyre circulation. This is particularly unfortunate for simulations of past climate states for which a millennial scale spin-up would be required. By affecting the formation and export of AABW, the spurious behaviour may create undesirable, long-lasting signals being stored for centuries in the deep ocean of the respective simulation. The set of experiments presented here indicate that even a significant reduction in the warm bias of the coarse resolution model may not be sufficient to keep the nested model from developing spurious behaviour. We therefore strongly advocate to initialise any high-resolution, eddying simulation of the SO from an ocean state based on observations. Our NOBIAS_N simulation suggests that even in this case a minimum of 100 years of spin-up are required.

Secondly, in a spun-up SO the amount of heat that is stored in the deep ocean is critical for the adjustment of the simulated climate to global warming scenarios. In general, a warmer SO, especially in the sub-surface, flattens the isopycnal sloping related to meridional upwelling, resulting in a weaker ACC and stronger subpolar gyres. Further north, the Agulhas current is stronger when the subsurface SO heat content is larger. Mesoscale eddies play a crucial role in determining stratification and ACC strength (e.g., Danabasoglu and McWilliams, 1995). This suggests a need for both improved observational coverage and further research enhancing our understanding of fundamental SO processes under climate change, aiming at an improved parameterisation of eddies. In general, high-resolution eddying simulations are much less prone to the typical warm bias found in many coarse-resolution model simulations. Our results demonstrate the importance to explicitly simulate mesoscale eddies for a more realistic representation of the SO in climate simulations. While some mesoscale processes can successfully be parameterised, such as mixing related to baroclinicity, others cannot, for instance, bottom water formation and Antarctic slope current dynamics.

Our study may serve as an example to guide a discussion on how to best implement and apply state-of-the-art high-resolution models to research questions of past and future climate change and the extent of a necessary model spin-up. As ocean model grids enabling eddy-rich simulations at the latitude of the ACC become more widely used, particular attention should be paid to the high latitude SO, where the grid resolution may only allow for large mesoscale features to be explicitly resolved. In this case, scale-aware or careful, spatially limited application of eddy parameterisations may lead to improved simulations.

CRediT authorship contribution statement

Mathias Zeller: Writing – review & editing, Writing – original draft, Visualization, Methodology, Investigation, Formal analysis, Data curation, Conceptualization. **Torge Martin:** Writing – review & editing, Investigation, Funding acquisition, Data curation, Conceptualization.

Declaration of competing interest

The authors declare that they have no known competing financial interests or personal relationships that could have appeared to influence the work reported in this paper.

Data availability

The data and material that support the findings of this study are available through GEOMAR at hdl:20.500.12085/25034230-5e36-435a-8939-44fe9f2fd35d (Zeller and Martin, 2024).

Supplementary data to Zeller and Martin (2024): On warm bias and m esoscale dynamics setting the Southern Ocean large-scale circulation m ean state. (Original data) (https://hdl.handle.net/20.500.12085/2503 4230-5e36-435a-8939-44fe9f2fd35d)

Acknowledgements

We thank Franziska Schwarzkopf and Sebastian Wahl for their support in setting up the model. We are also grateful for the helpful discussions with Joakim Kjellsson, Malin Ödalen and others of the FOCI development team at GEOMAR. Thanks also to Ilana Schiller-Weiss for proof-reading the manuscript. The comments by two anonymous reviewers were particularly helpful in improving the manuscript. This study was funded by the German Federal Ministry of Education and Research (BMBF) as a Research for Sustainability initiative (FONA) through the project PalMod: From the Last Interglacial to the Anthropocene – Modeling a Complete Glacial Cycle, Part 2; WP1.3.4: Role of mesoscale eddies in the Southern Ocean (FKZ: 01LP1918C). The model simulations were carried out at the center for National High Performance Computing, Zuse Institute Berlin (NHR@ZIB) providing computational resources and technical support (project *shk00044*).

References

Beadling, R., Russell, J., Stouffer, R., Mazloff, M., Talley, L., Goodman, P., Sallée, J., Hewitt, H., Hyder, P., Pandde, A., 2020. Representation of Southern Ocean properties across coupled model intercomparison project generations: CMIP3 to CMIP6. J. Clim. 33 (15), 6555–6581.

Behrens, E., Rickard, G., Morgenstern, O., Martin, T., Osprey, A., Joshi, M., 2016. Southern ocean deep convection in global climate models: A driver for variability of subpolar gyres and drake passage transport on decadal timescales. J. Geophys. Res.: Oceans 121 (6), 3905–3925.

Biastoch, A., Böning, C., Lutjeharms, J., 2008a. Agulhas leakage dynamics affects decadal variability in Atlantic overturning circulation. Nature 456 (7221), 489–492.

Biastoch, A., Lutjeharms, J., Böning, C., Scheinert, M., 2008b. Mesoscale perturbations control inter-ocean exchange south of Africa. Geophys. Res. Lett. 35 (20).

Chelton, D., Schlax, M., Samelson, R., 2011. Global observations of nonlinear mesoscale eddies. Prog. Oceanogr. 91 (2), 167–216.

Danabasoglu, G., McWilliams, J., 1995. Sensitivity of the global ocean circulation to parameterizations of mesoscale tracer transports. J. Clim. 8 (12), 2967–2987.

Debreu, L., Vouland, C., Blayo, E., 2008. AGRIF: Adaptive grid refinement in fortran. Comput. Geosci. 34 (1), 8–13.

Donohue, K., Tracey, K., Watts, D., Chidichimo, M., Chereskin, T., 2016. Mean antarctic circumpolar current transport measured in drake passage. Geophys. Res. Lett. 43 (22), 11,760 – 11,767.

Dufour, C., Morrison, A., Griffies, S., Frenger, I., Zanowski, H., Winton, M., 2017. Preconditioning of the Weddell Sea polynya by the ocean mesoscale and dense water overflows. J. Clim. 30 (19), 7719–7737.

Eyring, V., Bony, S., Meehl, G., Senior, C., Stevens, B., Stouffer, R., Taylor, K., 2016. Overview of the coupled model intercomparison project phase 6 (CMIP6) experimental design and organization. Geosci. Model Dev. 9 (5), 1937–1958.

Ferster, B., Subrahmanyam, B., Arguez, A., 2019. Recent changes in Southern Ocean circulation and climate. IEEE Geosci. Remote Sens. Lett. 16 (5), 667–671.

Fichefet, T., Morales Maqueda, M., 1997. Sensitivity of a global sea ice model to the treatment of ice thermodynamics and dynamics. J. Geophys. Res.: Oceans 102 (C6), 12609–12646.

Frenger, I., Münnich, M., Gruber, N., Knutti, R., 2015. Southern ocean eddy phenomenology. J. Geophys. Res.: Oceans 120 (11), 7413–7449.

Frölicher, T., Sarmiento, J., Paynter, D., Dunne, J., Krasting, J., Winton, M., 2015. Dominance of the Southern Ocean in anthropogenic carbon and heat uptake in CMIP5 models. J. Clim. 28 (2), 862–886.

Gent, P., McWilliams, J., 1990. Isopycnal mixing in ocean circulation models. J. Phys. Oceanogr. 20, 150–155.

Giorgetta, M., Jungclaus, J., Reick, C., Legutke, S., Bader, J., Böttinger, M., Brovkin, V., Crueger, T., Esch, M., Fieg, K., Glushak, K., Gayler, V., Haak, H., Hollweg, H.-D., Ilyina, T., Kinne, S., Kornblueh, L., Matei, D., Mauritsen, T., Mikolajewicz, U., Mueller, W., Notz, D., Pithan, F., Raddatz, T., Rast, S., Redler, R., Roeckner, E., Schmidt, H., Schnur, R., Segschneider, J., Six, K., Stockhause, M., Timmreck, C., Wegner, J., Widmann, H., Wieners, K.-H., Claussen, M., Marotzke, J., Stevens, B., 2013. Climate and carbon cycle changes from 1850 to 2100 in MPI-ESM simulations for the coupled model intercomparison project phase 5. J. Adv. Modelling Earth Syst. 5 (3), 572–597.

Gnanadesikan, A., Pradal, M.-A., Abernathey, R., 2015. Isopycnal mixing by mesoscale eddies significantly impacts oceanic anthropogenic carbon uptake. Geophys. Res. Lett. 42 (11), 4249–4255.

Gordon, A., 1986. Interocean exchange of thermocline water. J. Geophys. Res. 91, 5037–5050.

Griffies, S., Winton, M., Anderson, W., Benson, R., Delworth, T., Dufour, C., Dunne, J., Goddard, P., Morrison, A., Rosati, A., Wittenberg, A., Yin, J., Zhang, R., 2015. Impacts on ocean heat from transient mesoscale eddies in a hierarchy of climate models. J. Clim. 28 (3), 952–977.

Hallberg, R., 2013. Using a resolution function to regulate parameterizations of oceanic mesoscale eddy effects. Ocean Model. 72, 92–103.

Heuze, C., 2021. Antarctic bottom water and north Atlantic deep water in CMIP6 models. Ocean Sci. 17 (1), 59–90.

Heuze, C., Heywood, K., Stevens, D., Ridley, J., 2013. Southern ocean bottom water characteristics in CMIP5 models. Geophys. Res. Lett. 40 (7).

Heuze, C., Ridley, J., Calvert, D., Stevens, D., Heywood, K., 2015. Increasing vertical mixing to reduce Southern Ocean deep convection in NEMO3.4. Geosci. Model Dev. 8 (10), 3119–3130.

Ivanciu, I., Matthes, K., Biastoch, A., Wahl, S., Harlass, J., 2022. Twenty-first-century southern hemisphere impacts of ozone recovery and climate change from the stratosphere to the ocean. Weather Clim. Dyn. 3 (1), 139–171.

Johnson, G., Purkey, S., Toole, J., 2008. Reduced antarctic meridional overturning circulation reaches the north Atlantic ocean. Geophys. Res. Lett. 35 (22).

Kamenkovich, I.V., Sarachik, E.S., 2004. Mechanisms controlling the sensitivity of the Atlantic thermohaline circulation to the parameterization of eddy transports in ocean GCMs. J. Phys. Oceanogr. 34 (7), 1628–1647.

Khatiwala, S., Primeau, F., Hall, T., 2009. Reconstruction of the history of anthropogenic CO2 concentrations in the ocean. Nature 462 (7271), 346–349.

Kjellsson, J., Holland, P., Marshall, G., Mathiot, P., Aksenov, Y., Coward, A., Bacon, S., Megann, A., Ridley, J., 2015. Model sensitivity of the Weddell and Ross seas, Antarctica, to vertical mixing and freshwater forcing. Ocean Model. 94, 141–152.

Kjellsson, J., Wahl, S., Bischof, S., Kummer, L., Martin, T., Pilch Kedzierski, R., Zeller, M., Oedalen, M., Park, W., Reducing Southern Ocean biases in the FOCI climate model. J. Adv. Model. Earth Syst. subm.

Klatt, O., Fahrbach, E., Hoppema, M., Rohardt, G., 2005. The transport of the Weddell Gyre across the prime meridian. Deep-Sea Res. II: Top. Stud. Oceanogr. 52 (3–4), 513–528.

Koenig, Z., Provost, C., Ferrari, R., Sennéchael, N., Rio, M.-H., 2014. Volume transport of the Antarctic circumpolar current: Production and validation of a 20 year long time series obtained from in situ and satellite observations. J. Geophys. Res.: Oceans 119 (8), 5407–5433.

Levitus, S., 1998. World ocean data base 1998. In: NOAA Atlas NESDIS 18. p. 346.

Liau, J.-R., Chao, B.F., 2017. Variation of antarctic circumpolar current and its intensification in relation to the southern annular mode detected in the time-variable gravity signals by GRACE satellite 6. Geodesy. Earth Planets Space 69 (1).

Lu, J., Speer, K., 2010. Topography, jets, and eddy mixing in the Southern Ocean. J. Mar. Res. 68 (3–4), 479–502.

Lutjeharms, J., Vanballegooyen, R., 1988. The retroflection of the Agulhas current. J. Phys. Oceanogr. 18 (11), 1570–1583.

Ma, L., Wang, B., Cao, J., 2020. Impacts of atmosphere–sea ice–ocean interaction on Southern Ocean deep convection in a climate system model. Clim. Dyn. 54 (9–10), 4075–4093.

Madec, G., the NEMO team, 2016. NEMO ocean engine. p. 406, Note du Pôle modélisation, Inst. Pierre-Simon Laplace.

Marshall, J., Shuckburgh, E., Jones, H., Hill, C., 2006. Estimates and implications of surface eddy diffusivity in the southern ocean derived from tracer transport. J. Phys. Oceanogr. 36 (9), 1806–1821.

Martin, T., Biastoch, A., 2023. On the ocean's response to enhanced Greenland runoff in model experiments: relevance of mesoscale dynamics and atmospheric coupling. Ocean Sci. 19 (1), 141–167.

Martin, T., Park, W., Latif, M., 2013. Multi-centennial variability controlled by Southern Ocean convection in the Kiel climate model. Clim. Dyn. 40 (7–8), 2005–2022.

Martin, T., Zeller, M., Processes determining Antarctic Circumpolar Current strength in a climate model with eddying Southern Ocean. Geophys. Res. Lett. subm.

Matthes, K., Biastoch, A., Wahl, S., Harlass, J., Martin, T., Brücher, T., Drews, A., Ehlert, D., Getzlaff, K., Krüger, F., Rath, W., Scheinert, M., Schwarzkopf, F., Bayr, T., Schmidt, H., Park, W., 2020. The flexible ocean and climate infrastructure version 1 (FOCI1): Mean state and variability. Geosci. Model Dev. 13 (6), 2533–2568.

McCann, M., Semtner, A., Chervin, R., 1994. Transports and budgets of volume, heat, and salt from a global eddy-resolving ocean model. Clim. Dyn. 10 (1–2), 59–80.

Meijers, A., Shuckburgh, E., Bruneau, N., Sallee, J.-B., Bracegirdle, T., Wang, Z., 2012. Representation of the antarctic circumpolar current in the CMIP5 climate models and future changes under warming scenarios. J. Geophys. Res.: Oceans 117 (12).

Morrison, A., Griffies, S., Winton, M., Anderson, W., Sarmiento, J., 2016. Mechanisms of Southern Ocean heat uptake and transport in a global eddying climate model. J. Clim. 29 (6), 2059–2075.

Morrison, A., Hogg, A., 2013. On the relationship between Southern Ocean overturning and ACC transport. J. Phys. Oceanogr. 43 (1), 140–148.

Morrow, R., Coleman, R., Church, J., Chelton, D., 1994. Surface eddy momentum flux and velocity variances in the Southern Ocean from geosat altimetry. J. Phys. Oceanogr. 24 (10), 2050–2071.

Nikurashin, M., Vallis, G., 2012. A theory of the interhemispheric meridional overturning circulation and associated stratification. J. Phys. Oceanogr. 42 (10), 1652–1667.

Orsi, A., Johnson, G., Bullister, J., 1999. Circulation, mixing, and production of antarctic bottom water. Prog. Oceanogr. 43 (1), 55–109.

Patara, L., Boening, C., Biastoch, A., 2016. Variability and trends in Southern Ocean eddy activity in 1/12° ocean model simulations. Geophys. Res. Lett. 43 (9), 4517–4523.

Rae, J., Burke, A., Robinson, L., Adkins, J., Chen, T., Cole, C., Greenop, R., Li, T., Littley, E., Nita, D., Stewart, J., Taylor, B., 2018. CO2 storage and release in the deep Southern Ocean on millennial to centennial timescales. Nature 562 (7728), 569–573.

Roberts, M., Baker, A., Blockley, E., Calvert, D., Coward, A., Hewitt, H., Jackson, L., Kuhlbrodt, T., Mathiot, P., Roberts, C., Schiemann, R., Seddon, J., Vannière, B., Luigi Vidale, P., 2019. Description of the resolution hierarchy of the global coupled HadGEM3-GC3.1 model as used in CMIP6 HighResMIP experiments. Geosci. Model Dev. 12 (12), 4999–5028.

Schmitz, W., 1996. On the World Ocean Circulation. Volume 1. Some Global Features / North Atlantic Circulation. Technical Report, WHOI-96-03, p. 140.

Schulzki, T., Harlass, J., Schwarzkopf, F., Biastoch, A., 2022. Toward ocean hindcasts in earth system models: AMOC variability in a partially coupled model at eddying resolution. J. Adv. Modelling Earth Syst. 14 (12), e2022MS003200, e2022MS003200 2022MS003200.

Silvano, A., Purkey, S., Gordon, A., Castagno, P., Stewart, A., Rintoul, S., Foppert, A., Gunn, K., Herraiz-Borreguero, L., Aoki, S., Nakayama, Y., Naveira Garabato, A., Spingys, C., Akhoudas, C., Sallée, J.-B., de Lavergne, C., Abrahamsen, E., Meijers, A., Meredith, M., Zhou, S., Tamura, T., Yamazaki, K., Ohshima, K., Falco, P., Budillon, G., Hattermann, T., Janout, M., Llanillo, P., Bowen, M., Darelius, E., Osterhus, S., Nicholls, K., Stevens, C., Fernandez, D., Cimoli, L., Jacobs, S., Morrison, A., Hogg, A., Haumann, A., Mashayek, A., Wang, Z., Kerr, R., Williams, G., Lee, W., 2023. Observing antarctic bottom water in the Southern Ocean. Front. Mar. Sci. 10.

Singh, H., Goldenson, N., Fyfe, J., Polvani, L., 2023. Uncertainty in preindustrial global ocean initialization can yield irreducible uncertainty in Southern Ocean surface climate. J. Clim. 36 (2), 383–403.

Solodoch, A., Stewart, A., Hogg, A., Morrison, A., Kiss, A., Thompson, A., Purkey, S., Cimoli, L., 2022. How does antarctic bottom water cross the Southern Ocean? Geophys. Res. Lett. 49 (7).

Sonnewald, M., Reeve, K., Lguensat, R., 2023. A Southern Ocean supergyre as a unifying dynamical framework identified by physics-informed machine learning. Commun. Earth Environ. 4 (1).

Speich, S., Blanke, B., Cai, W., 2007. Atlantic meridional overturning circulation and the southern hemisphere supergyre. Geophys. Res. Lett. 34 (23).

Stammer, D., 1998. On eddy characteristics, eddy transports, and mean flow properties. J. Phys. Oceanogr. 28 (4), 727–739.

Steele, M., Morley, R., Ermold, W., 2001. PHC: A global ocean hydrography with a high-quality arctic ocean. J. Clim. 14 (9), 2079–2087.

Stevens, B., Giorgetta, M., Esch, M., Mauritsen, T., Crueger, T., Rast, S., Salzmann, M., Schmidt, H., Bader, J., Block, K., Brokopf, R., Fast, I., Kinne, S., Kornblueh, L., Lohmann, U., Pincus, R., Reichler, T., Roeckner, E., 2013. Atmospheric component of the MPI-M earth system model: ECHAM6. J. Adv. Modelling Earth Syst. 5 (2), 146–172.

Talley, L., 2013. Closure of the global overturning circulation through the Indian, Pacific, and Southern Oceans. Oceanography 26 (1), 80–97.

Tan, S., Thurnherr, A., 2023. On the global decrease in the deep and abyssal density stratification along the spreading pathways of antarctic bottom water since the 1990s. Geophys. Res. Lett. 50 (11), e2022GL102422, e2022GL102422 2022GL102422.

Toggweiler, J.R., Samuels, B., 1998. On the ocean's large-scale circulation near the limit of no vertical mixing. J. Phys. Oceanogr. 28 (9), 1832–1852.

Treguier, A., Deshayes, J., Lique, C., Dussin, R., Molines, J., 2012. Eddy contributions to the meridional transport of salt in the north Atlantic. J. Geophys. Res.: Oceans 117.

Treguier, A., Held, I., Larichev, V., 1997. Parameterization of quasigeostrophic eddies in primitive equation ocean models. J. Phys. Oceanogr. 27 (4), 567–580.

Valcke, S., Craig, A., Dunlap, R., Riley, G., 2016. Sharing experiences and outlook on coupling technologies for earth system models. Bull. Am. Meteorol. Soc. 97 (3), ES53–ES56.

Vargas-Alema, J., Vigo, M., Garcia-Garcia, D., Zid, F., 2023. Updated geostrophic circulation and volume transport from satellite data in the Southern Ocean. Front. Earth Sci. 11, 1110138.

Vernet, M., Geibert, W., Hoppema, M., Brown, P., Haas, C., Hellmer, H., Jokat, W., Jullion, L., Mazloff, M., Bakker, D., Brearley, J., Croot, P., Hattermann, T., Hauck, J., Hillenbrand, C.-D., Hoppe, C., Huhn, O., Koch, B., Lechtenfeld, O., Meredith, M., Naveira Garabato, A., Nöthig, E.-M., Peeken, I., Rutgers van der Loeff, M., Schmidtko, S., Schröder, M., Strass, V., Torres-Valdés, S., Verdy, A., 2019. The Weddell Gyre, Southern Ocean: Present knowledge and future challenges. Rev. Geophys. 57 (3), 623–708.

Wang, Y., Heywood, K., Stevens, D., Damerell, G., 2022. Seasonal extrema of sea surface temperature in CMIP6 models. Ocean Sci. 18 (3), 839–855.

Wang, C., Zhang, L., Lee, S., Wu, L., Mechoso, C., 2014. A global perspective on CMIP5 climate model biases. Nature Clim. Change 4 (3), 201–205.

Xu, X., Chassignet, E., Firing, Y., Donohue, K., 2020. Antarctic circumpolar current transport through drake passage: What can we learn from comparing high-resolution model results to observations? J. Geophys. Res.: Oceans 125 (7), e2020JC016365, e2020JC016365 2020JC016365.

Zanna, L., Khatiwala, S., Gregory, J., Ison, J., Heimbach, P., 2019. Global reconstruction of historical ocean heat storage and transport. Proc. Natl. Acad. Sci. USA 116 (4), 1126–1131.

Zeller, M., Martin, T., 2024. Supplementary data to Zeller and Martin (2024): On warm bias and mesoscale dynamics setting the Southern Ocean large-scale circulation mean state. GEOMAR Helmholtz Cent. Ocean Res. Kiel https://hdl.handle.net/20.500.12085/25034230-5e36-435a-8939-44fe9f2fd35d.

Zhang, H., Whalen, C., Kumar, N., Purkey, S., 2021. Decreased stratification in the abyssal southwest Pacific basin and implications for the energy budget. Geophys. Res. Lett. 48 (19), e2021GL094322, e2021GL094322 2021GL094322.

Zhou, S., Meijers, A., Meredith, M., Abrahamsen, E., Holland, P., Silvano, A., Sallee, J.-B., Osterhus, S., 2023. Slowdown of antarctic bottom water export driven by climatic wind and sea-ice changes. Nature Clim. Change 13 (7), 701+.